Studia Geophysica & Geodetica (preprint)

Modelling converted seismic waveforms in isotropic and anisotropic 1–D gradients: discontinuous versus continuous gradient representations

D.A. Angus[1] & C.J. Thomson[2]

[1] *School of Earth & Environment, University of Leeds, Leeds, d.angus@leeds.ac.uk*
[2] *Schlumberger Cambridge Research, Cambridge, UK*

Accepted: Studia Geophysica & Geodetica: 2012

Abstract
Over the past decade, there have been numerous receiver function studies directed at imaging the lithosphere–asthenosphere boundary (LAB). Although it is generally accepted that receiver function phases observed in these studies are derived from physical mode conversions at depth within the lithosphere–asthenosphere transition, it is still debatable as to whether these phases are directly indicative of the LAB. This is because interpretation of receiver function LAB signals relies on understanding the elastic characteristics of the Earth's outer thermal boundary layer. The main issues for receiver function imaging are the sharpness of the elastic material property transition and, more importantly, what specifically are the material gradients. To test the various transition models, a forward modelling approach is required that allows accurate waveform synthetics for a range of discontinuous and continuous gradients in anisotropic, elastic media. We present a derivation of the reflection and transmission response for continuous one–dimensional (1–D) gradients in generally anisotropic elastic media. We evaluate the influence of 1–D isotropic and anisotropic elastic gradients on the seismic waveform by comparing numerical results of models for discontinuous and continuous transitions. The results indicate that discontinuous representations using layers each with uniform parameters and with thicknesses on the order of approximately 1/3 to 1/8 of the dominant seismic wavelength can be used to accurately model P–to–S and S–to–P mode conversions due to continuous transitions of both isotropic and anisotropic elastic properties. From a practical point of view, when comparing synthetic modelling with observation, this constraint can be relaxed further. The presence of signal noise and/or the result of receiver function stacking techniques will likely obscure these subtle waveform effects. Hence this study suggest that accurate synthetic waveforms for LAB transitions can be modelled with discontinuous gradient representations using a reasonable number of discrete transition layers with layer thicknesses no greater than 1/2 to 1/3 the dominant seismic wavelength.

Key words: elastic waves, isotropic and anisotropic gradients, lithosphere–asthenosphere boundary, reflection and transmission response, Ricatti equations.

1 INTRODUCTION

The Earth is elastically anisotropic and heterogeneous over a wide range of scales and this complexity is manifested in the numerous seismic phases and their waveforms from earthquakes. As such, analysis of teleseismic waves has become a fundamental component of global Earth studies, providing constraints on the Earth's geometry as well as thermal and chemical evolution. Due to economic and practical limitations on the location and size of seismic arrays as well as the uneven distribution of earthquake sources, interpretation of teleseismic observables is inherently non–unique. Integrating teleseismic observations with forward modelling enables one to reduce the non–uniqueness of the solution and aid interpretation by testing various hypotheses and models (e.g., Hammond et al., 2010). Since there is no general analytic solution to the elastic wave equation for anisotropic and heterogeneous media, the choice of forward modelling algorithm generally involves one or more approximations based on physically motivated arguments specific to the problem under study. Often this is done by reducing the complex-

ity of the model, for example, a reduction from elastic to acoustic media (e.g., Brenders & Pratt, 2007).

Although the Earth is heterogeneous in all three–dimensions, in a broad sense and on a global scale this heterogeneity is predominantly depth dependent as a result of the pressure and temperature distribution within the Earth. Teleseismic mode conversions from P– and S–wave phases are ideal for studying depth dependent structure in the crust and upper mantle (e.g., Vinnik, 1977). By removing source and receiver side waveform effects via deconvolution, the receiver function method (e.g., Langston, 1977) enhances any sub–vertically propagating mode conversions (i.e., P–to–S and S–to–P) and hence enables relatively high resolution vertical and potentially lateral imaging of crustal (e.g., Tomlinson et al., 2003; Angus et al., 2009) and upper–mantle discontinuities (e.g., Helffrich et al., 2003; Thompson et al., 2011). Since receiver function analysis focusses primarily on vertical structure, a reduction of the model space from three dimensions (3–D) to one–dimension (1–D) allows for a more tractable solution of the wave physics of interest (i.e., mode conversions). Reflectivity modelling [either considering a spectrum of slownesses (e.g., Fuchs & Mueller, 1971) or the plane–wave response (e.g., Frederiksen & Bostock, 2000)], is often the forward modelling tool of choice in the interpretation of receiver functions and this is because it is computationally efficient and yields accurate full waveform solutions. However, more advanced methods, such as one–way wave equation techniques, are now being applied that allow for lateral variations in the topology of sub–horizontal crustal and upper–mantle discontinuities within the model (e.g., Audet et al., 2007).

Over the past decade, there has been significant interest in imaging the lithosphere–asthenosphere boundary (LAB) (see Fischer et al., 2010, and references therein). However, the exact definition of the lithosphere and the asthenosphere varies within the geoscience community and hence a ubiquitous definition of the LAB remains controversial (see Artemieva, 2009). In a general sense, the LAB represents the boundary or transition within the upper mantle between the convective asthenosphere and the conductive lithosphere. Regardless of the semantics involved in defining the LAB, the geophysical characteristics of this transition have important implications on our understanding of upper–mantle convection, the outer thermal boundary layer and the evolution of plate tectonics.

Receiver function analyses using teleseismic P–to–S and S–to–P mode conversions have been used to delineate sharp sub–horizontal seismic discontinuities generally inferred to be the LAB (e.g., Farra & Vinnik, 2000; Li et al., 2004; Kumar et al., 2005; Rychert et al., 2005; Angus et al., 2006). In some instances, however, receiver function interpretations of the LAB have been at odds with other geophysical data, such as mantle xenolith thermal studies (Tommasi, personal communication, 2007). This suggests a better understanding of the mechanisms leading to mode conversions at these depths and more concrete evidence to indicate whether the converted phases are truly related to the LAB, or not, is needed. Thermal models suggest a very weak and diffuse LAB leading to predicted low amplitude and broad converted seismic waves, and hence are inconsistent with receiver function studies. However, current hypotheses suggest that seismic waves within this thermal transition are sensitive to much sharper contrasts in elastic properties, such as changes in mantle hydration, chemical fertility, melt content and/or vertical gradients in elastic anisotropy (e.g., Artemieva, 2009; Fischer et al., 2010; Holtzman & Kendall, 2010). Thus, elastic gradients associated with the thermal LAB can be expected to range from smooth to relatively sharp.

2 STATEMENT OF PROBLEM

The receiver function method provides an estimate of the Earth structure in terms of a sequence of time offset mode conversions from sub-horizontal discontinuities and hence the assumption of predominantly 1–D vertical structure for individual receiver functions is generally sufficient. To correctly model the seismic response due to 1–D structure one needs to consider the interaction of the incident elastic wave with a discontinuity in material properties. The energy of the primary wave can be converted into up to six secondary waves. Although Snell's law can be used to determine the directional properties of all the secondary waves, it cannot provide information on waveform amplitudes and pulse distortion. Thus a more complete evaluation of the reflection and transmission (R/T) properties is needed. Over the past several decades significant contributions have been made in the evaluation of R/T coefficients for isotropic (e.g., Gilbert & Backus, 1983; Molotkov et al., 1976; Novotný et al., 1980; Kennett, 1983) and anisotropic (e.g., Garmany, 1983; Fryer & Frazer, 1984; Guest et al., 1993) layered media (see Kennett, 2001a). In most of these approaches, the solution to the R/T response involves using a local plane–wave and plane–boundary approximation (see Hudson, 1980; Kennett, 1983). The plane–wave R/T coefficients depend only on the slownesses, polarizations, and material properties at the point of incidence.

Since seismic signals are band limited, the length scale of heterogeneities can significantly influence the seismic wavefront and waveforms (e.g., Angus, 2005). For 1–D gradients, this scale dependence can have significant impact on the converted seismic waveform (e.g., Bostock, 1999; Angus, 2007). When the length scale of a transition in elastic properties is much smaller than the seismic wavelength, the transmitted and reflected waveforms experience minimal distortion (i.e., they have essentially identical frequency content) and the transition can be best characterized by a discontinuous transition (i.e., a jump in material properties). However, when the length scale of a transition is comparable or larger in size than the seismic wavelength the transmitted and reflected waveforms can be modified significantly depending on the magnitude of elastic property perturbations. Smooth continuous gradients with transitions lengths on the order of the seismic wavelength are often modelled by a transition of many incremental discontinuities that approximate the smooth transition. For the isotropic case, a general rule-of-thumb is that a continuous transition can be subdivided into discrete layers with thickness on the order of 1/8 the seismic wavelength (e.g., see Kuhn, 1988, for the reflection problem) or less and yield sufficiently accurate solutions. Although this has been shown to produce accurate waveforms for isotropic gradients, is it a suitable approach for anisotropic gradients? For instance, anisotropic gradi-

ents have been shown to yield substantially complex waveform coupling (e.g., Shearer & Chapman, 1988; Chapman & Shearer, 1989; Coates & Chapman, 1990, to name just a few studies), but how this might impact on mode conversions and receiver functions has yet to be examined.

In this paper, we present a derivation of the R/T response for 1–D, continuously–varying, generally anisotropic elastic media and evaluate the influence of 1–D isotropic and anisotropic elastic gradients on the seismic waveform. Specifically, we compare numerical results for 1–D discontinuous and continuous transitions for both isotropic and anisotropic media. The concepts presented here were initially based on Kennett (1983) for the isotropic elastic case and contributions from Thomson (1996b) for both the anisotropic discontinuous elastic case as well as the isotropic and anisotropic continuous elastic case. The reader is referred to Kennett (2001a) for a more current overview of R/T theory and Kennett (2001b) for application of modelling to teleseismic data.

3 REFLECTION AND TRANSMISSION COEFFICIENTS

The theory presented here is expressed in Cartesian coordinates $(x_1, x_2, x_3) = (x, y, z)$ with z positive downwards and summation convention implied. For an elastic medium, the linear stress–strain relation is

$$\sigma_{ij} = c_{ijkl} \frac{\partial u_k}{\partial x_l} \ , \tag{3.1}$$

where c_{ijkl} is the fourth–order tensor of elastic parameters, σ_{ij} is the stress tensor, $\epsilon_{kl} = \partial u_k / \partial x_l$ is the strain tensor, u_k is the k–th component of displacement, and x_l is the l–th Cartesian coordinate. For an impulsive point force with magnitude m_i, located spatially and temporally at $\mathbf{x}^\dagger$ and $t^\dagger$, the equation of motion is

$$\frac{\partial \sigma_{ij}}{\partial x_j} = \rho \frac{\partial^2 u_i}{\partial t^2} + m_i \delta(\mathbf{x} - \mathbf{x}^\dagger) \delta(t^\dagger) \ , \tag{3.2}$$

where ρ is density. For 1–D media, the material properties vary only with depth z and so the source is defined at $\mathbf{x}^\dagger = (0, 0, x_3^\dagger)$.

The 3–D Fourier transform of the displacement wavefield $\mathbf{u}$ is expressed with respect to time and lateral coordinates

$$\begin{aligned} u(p_1, p_2, \omega) \quad = \quad & \int\int\int_{-\infty}^{\infty} u(x_1, x_2, t) \\ & \mathrm{e}^{[-\mathrm{i}\omega(p_1 x_1 + p_2 x_2 - t)]} dx_1 dx_2 dt \ , \end{aligned} \tag{3.3}$$

where p_1, p_2 are the lateral slowness and $u(x_1, x_2, t) = u(x_3) \mathrm{e}^{[-\mathrm{i}\omega(p_1 x_1 + p_2 x_2 - t)]}$ is the plane–wave solution for frequency ω. From here on, the lateral coordinates and slownesses are denoted by Greek subscripts (e.g., x_α and p_α). After Fourier transformation and using a modified form introduced by Woodhouse (1973), the equation of motion 3.2 is written in matrix form (Guest et al., 1993)

$$\frac{d\mathbf{y}}{dx_3} = \mathrm{i}\omega \mathbf{A}\mathbf{y} + \mathbf{s}\delta(x_3 - x_3^\dagger) \mathrm{e}^{-\mathrm{i}\omega p_\alpha x_\alpha} \ , \tag{3.4}$$

where the 6–vector

$$\mathbf{y} = \begin{pmatrix} u_i \\ t_i \end{pmatrix} \tag{3.5}$$

consists of components of displacement u_i and normal traction t_i

$$u_i = (u_1, u_2, u_3)^T \quad \text{and} \quad t_i = \frac{1}{\mathrm{i}\omega} (\sigma_{13}, \sigma_{23}, \sigma_{33})^T \ . \tag{3.6}$$

The system matrix $\mathbf{A}$ is partitioned into four 3×3 matrices as follows:

$$\mathbf{A} = \begin{pmatrix} \mathbf{T}^T & \mathbf{C}_{33}^{-1} \\ \mathbf{S} & \mathbf{T} \end{pmatrix} \ , \tag{3.7}$$

where

$$\mathbf{T} = -p_\gamma \mathbf{C}_{\gamma 3} \mathbf{C}_{33}^{-1} \tag{3.8}$$

and

$$\mathbf{S} = \rho \mathbf{I} - p_\gamma p_\alpha \left(\mathbf{C}_{\alpha\gamma} - \mathbf{C}_{\alpha 3} \mathbf{C}_{33}^{-1} \mathbf{C}_{3\gamma} \right) \ . \tag{3.9}$$

The reduced elasticity matrix C_{ij} is defined $(C_{ik})_{jl} = c_{ijkl}$ (e.g., $C_{33} = c_{i3k3}$). The 6×6 system matrix $\mathbf{A}$ is of particular importance because its eigenvectors define the displacements and interface tractions associated with all possible wavetypes. The corresponding six eigenvalues of $\mathbf{A}$ represent the six possible normal slownesses (p_3) to the interface for given lateral slownesses (p_α).

The expected solution in a homogeneous layer takes the form

$$\mathbf{y}(z) = \mathbf{N} \mathrm{e}^{\mathrm{i}\omega \mathbf{q} z} \mathbf{c} \ , \tag{3.10}$$

where $\mathbf{N}$ is a 6×6 matrix whose columns are the eigenvectors of $\mathbf{A}$, $\mathbf{q}$ is a diagonal matrix consisting of the corresponding eigenvalues and $\mathbf{c}$ is a column vector representing the wavevector constants for the layer defining the amplitudes of the upgoing and downgoing waves (assumed order as that of the columns of $\mathbf{N}$).

3.1 1–D discontinuous gradients

For elastic wave propagation, we require continuity of displacement and normal stresses across a material interface. For a single (horizontal) interface, the boundary conditions state that the wavevector z_1^+ just above the interface and z_1^- just below the interface are related by

$$\mathbf{N}(z_+)\mathbf{c}_+ = \mathbf{N}(z_-)\mathbf{c}_- \ , \tag{3.11}$$

neglecting the exponential term. Equation 3.11 can be applied to the set of all possible incident waves qP, qS_1 and qS_2 (q referring to quasi and indicating that the P–wave particle motion is not normal to the wavefront and that the S–wave motion is not parallel to the wavefront) at the interface and expressed in matrix form as

$$\mathbf{N}(z_+) \begin{pmatrix} \mathbf{0} & \mathbf{I} \\ \mathbf{T}_U & \mathbf{R}_D \end{pmatrix} = \mathbf{N}(z_-) \begin{pmatrix} \mathbf{R}_U & \mathbf{T}_D \\ \mathbf{I} & \mathbf{0} \end{pmatrix} \ , \tag{3.12}$$

where D refers to downward incident waves and U to upward incident waves (see Figure 1). For example, $\mathbf{T}_U$ is a 3×3 matrix of transmission coefficients for all three possible transmitted waves from the three possible upgoing incident waves.

Rearranging equation 3.12, a 6×6 layer interface scattering matrix $\mathbf{Q}$ is written

$$\begin{aligned} \mathbf{N}^{-1}(z_-)\mathbf{N}(z_+) \quad &= \quad \mathbf{Q}(z_-, z_+) \\ &= \quad \begin{pmatrix} \mathbf{T}_D - \mathbf{R}_U \mathbf{T}_U^{-1} \mathbf{R}_D & \mathbf{R}_U \mathbf{T}_U^{-1} \\ -\mathbf{T}_U^{-1} \mathbf{R}_D & \mathbf{T}_U^{-1} \end{pmatrix} . \end{aligned} \tag{3.13}$$

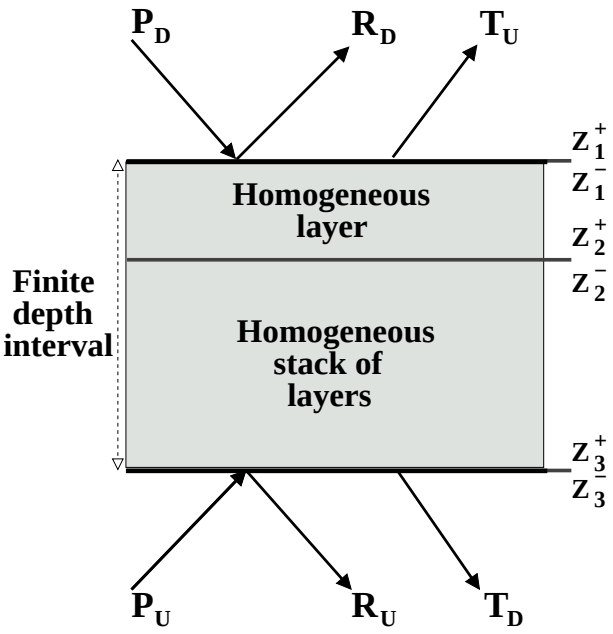

Figure 1. Cartoon of reflection and transmission matrix coefficients for a finite depth interval of a homogeneous stack of horizontal layers. R_D and T_D represent the reflected and transmitted plane wave from the locally plane wave P_D initially traveling downward. R_U and T_U represent the reflected and transmitted plane wave from the locally plane wave P_U initially traveling upward (Fryer & Frazer, 1984).

The wave propagator matrix $\mathbf{Q}$ is an expression of all the wavevectors in the upper and lower medium. The matrix $\mathbf{Q}$ can be inverted to express the 3×3 R/T matrices in terms of the 3×3 partitions of the scattering matrix denoted $\mathbf{Q}_{11}$, $\mathbf{Q}_{12}$, $\mathbf{Q}_{21}$, and $\mathbf{Q}_{22}$, as

$$\begin{pmatrix} \mathbf{T}_U & \mathbf{R}_U \\ \mathbf{R}_D & \mathbf{T}_D \end{pmatrix} = \begin{pmatrix} \mathbf{Q}_{22}^{-1} & \mathbf{Q}_{12}\mathbf{Q}_{22}^{-1} \\ -\mathbf{Q}_{22}^{-1}\mathbf{Q}_{21} & \mathbf{Q}_{11} - \mathbf{Q}_{12}\mathbf{Q}_{22}^{-1}\mathbf{Q}_{21} \end{pmatrix} \quad (3.14)$$

For a stack of homogeneous layers (see Figure 1), equation 3.11 can be generalized for a finite depth interval (z_3, z_2) as

$$\mathbf{N}(z_3)\mathbf{c}_3 = \mathbf{P}(z_3, z_2)\mathbf{N}(z_2)\mathbf{c}_2 \ , \quad (3.15)$$

where $\mathbf{P}$ is the displacement–stress propagator within the finite depth interval. The wavevectors $\mathbf{c}_2$ and $\mathbf{c}_3$ are related by the layer–interface scattering matrix

$$\begin{aligned} \mathbf{Q}(z_3, z_2) &= \mathbf{N}^{-1}(z_3)\mathbf{P}(z_3, z_2)\mathbf{N}(z_2) \quad (3.16) \\ &= \begin{pmatrix} \mathbf{T}_D - \mathbf{R}_U\mathbf{T}_U^{-1}\mathbf{R}_D & \mathbf{R}_U\mathbf{T}_U^{-1} \\ -\mathbf{T}_U^{-1}\mathbf{R}_D & \mathbf{T}_U^{-1} \end{pmatrix} , \end{aligned}$$

where the R/T matrices are those for the entire region between z_2 and z_3, whether it be one homogeneous layer or a finite stack of layers. Since the propagator $\mathbf{P}$ is in itself a product of individual propagators for each layer, it follows that the wave propagator satisfies the chain rule

$$\mathbf{Q}(z_3, z_1) = \mathbf{Q}(z_3, z_2)\mathbf{Q}(z_2, z_1) \ . \quad (3.17)$$

For a homogeneous layer of thickness $h = z_3 - z_2$ the wave propagator $\mathbf{Q}(z_3, z_2)$ can be expressed as

$$\mathbf{E}(z_3, z_2) = \begin{pmatrix} \mathbf{E}_D & 0 \\ 0 & \mathbf{E}_U \end{pmatrix} \quad (3.18)$$

where

$$\mathbf{E}_D = \mathrm{diag}\left[e^{i\omega q_{D_1} h}, e^{i\omega q_{D_2} h}, e^{i\omega q_{D_3} h}\right]$$

and

$$\mathbf{E}_U = \mathrm{diag}\left[e^{i\omega q_{U_1} h}, e^{i\omega q_{U_2} h}, e^{i\omega q_{U_3} h}\right] \ .$$

This represents a phase lag with no amplitude modification.

Using the chain rule 3.17, the R/T matrix coefficients for the depth interval below the interface z_1 to the base of interface z_3 (i.e., the region between z_1^- and z_3^- in Figure 1) can be expressed

$$\begin{pmatrix} \bar{\mathbf{T}}_D - \bar{\mathbf{R}}_U\bar{\mathbf{T}}_U^{-1}\bar{\mathbf{R}}_D & \bar{\mathbf{R}}_U\bar{\mathbf{T}}_U^{-1} \\ -\bar{\mathbf{T}}_U^{-1}\bar{\mathbf{R}}_D & \bar{\mathbf{T}}_U^{-1} \end{pmatrix} = \quad (3.19)$$
$$\begin{pmatrix} \mathbf{T}_D - \mathbf{R}_U\mathbf{T}_U^{-1}\mathbf{R}_D & \mathbf{R}_U\mathbf{T}_U^{-1} \\ -\mathbf{T}_U^{-1}\mathbf{R}_D & \mathbf{T}_U^{-1} \end{pmatrix} \begin{pmatrix} \mathbf{E}_D & 0 \\ 0 & \mathbf{E}_U \end{pmatrix} .$$

where the matrices with single overbars represent the R/T properties for the region (z_1^-, z_3^-). The R/T matrices without overbars represent those for region (z_2^+, z_3^-) and the far right matrices propagate the waves across the homogeneous region (z_1^-, z_2^+). With further simplification, the addition rules for adding a new layer to the stack (not including the top of the interface) can be expressed as

$$\begin{aligned} \bar{\mathbf{T}}_U &= \mathbf{E}_U^{-1}\mathbf{T}_U \\ \bar{\mathbf{R}}_D &= \mathbf{E}_U^{-1}\mathbf{R}_D\mathbf{E}_D \\ \bar{\mathbf{R}}_U &= \mathbf{R}_U \\ \bar{\mathbf{T}}_D &= \mathbf{T}_D\mathbf{E}_D \ . \quad (3.20) \end{aligned}$$

To include the top of interface z_1 (i.e., z_1^- to z_1^+), application of the chain rule gives

$$\begin{pmatrix} \tilde{\mathbf{T}}_D - \tilde{\mathbf{R}}_U\tilde{\mathbf{T}}_U^{-1}\tilde{\mathbf{R}}_D & \tilde{\mathbf{R}}_U\tilde{\mathbf{T}}_U^{-1} \\ -\tilde{\mathbf{T}}_U^{-1}\tilde{\mathbf{R}}_D & \tilde{\mathbf{T}}_U^{-1} \end{pmatrix} =$$
$$\begin{pmatrix} \bar{\mathbf{T}}_D - \bar{\mathbf{R}}_U\bar{\mathbf{T}}_U^{-1}\bar{\mathbf{R}}_D & \bar{\mathbf{R}}_U\bar{\mathbf{T}}_U^{-1} \\ -\bar{\mathbf{T}}_U^{-1}\bar{\mathbf{R}}_D & \bar{\mathbf{T}}_U^{-1} \end{pmatrix}$$
$$\begin{pmatrix} \mathbf{T}_D - \mathbf{R}_U\mathbf{T}_U^{-1}\mathbf{R}_D & \mathbf{R}_U\mathbf{T}_U^{-1} \\ -\mathbf{T}_U^{-1}\mathbf{R}_D & \mathbf{T}_U^{-1} \end{pmatrix} , \quad (3.21)$$

where the matrices to the left of the equality (i.e., with tildes) represent the R/T matrix coefficients for the whole region (z_1^+, z_3^-) and those to the right for the single interface (z_1^+, z_1^-) and stack region (z_1^-, z_3^-). Thus, the addition rules for including the new interface are

$$\begin{aligned} \tilde{\mathbf{T}}_U &= \mathbf{T}_U(\mathbf{I} - \bar{\mathbf{R}}_D\mathbf{R}_U)^{-1}\bar{\mathbf{T}}_U, \quad (3.22) \\ \tilde{\mathbf{T}}_D &= \bar{\mathbf{T}}_D[\mathbf{I} + \mathbf{R}_U(\mathbf{I} - \bar{\mathbf{R}}_D\mathbf{R}_U)^{-1}\bar{\mathbf{R}}_D]\mathbf{T}_D \\ &= \bar{\mathbf{T}}_D(\mathbf{I} - \mathbf{R}_U\bar{\mathbf{R}}_D)^{-1}\mathbf{T}_D, \quad (3.23) \\ \tilde{\mathbf{R}}_U &= \bar{\mathbf{R}}_U + \bar{\mathbf{T}}_D\mathbf{R}_U(\mathbf{I} - \bar{\mathbf{R}}_D\mathbf{R}_U)^{-1}\bar{\mathbf{T}}_U \\ &= \bar{\mathbf{R}}_U + \bar{\mathbf{T}}_D(\mathbf{I} - \mathbf{R}_U\bar{\mathbf{R}}_D)^{-1}\mathbf{R}_U\bar{\mathbf{T}}_U, \quad (3.24) \\ \tilde{\mathbf{R}}_D &= \mathbf{R}_D + \mathbf{T}_U(\mathbf{I} - \bar{\mathbf{R}}_D\mathbf{R}_U)^{-1}\bar{\mathbf{R}}_D\mathbf{T}_D \\ &= \mathbf{R}_D + \mathbf{T}_U\bar{\mathbf{R}}_D(\mathbf{I} - \mathbf{R}_U\bar{\mathbf{R}}_D)^{-1}\mathbf{T}_D \ . \quad (3.25) \end{aligned}$$

The addition rules are well known (Kennett, 1974; Saastamoinen, 1980; Ursin, 1983) and are a consequence of the

invariant bedding approach in the derivation of the reflection and transmission coefficients.

3.2 1–D continuous gradients

The R/T solution for continuous or higher order transitions can be approximated by dividing the transition zone into many thin homogeneous layers when the material gradients are high (Haskell, 1953; Gilbert & Backus, 1983). Another approach is to apply a phase shift neglecting amplitude effects when the material gradients are small (Helffrich et al., 2008); there is minimal amplitude error when the material gradients are weak (Angus, 2004). Although this might be an efficient approach for isotropic gradients, the question remains as to whether it is suitable for anisotropic transitions that might arise, for instance, due to melt or strain induced anisotropy related to the Earth's depth dependent geotherm. In this section, we introduce a formulation for the R/T response for a continuous 1–D transition. This approach is similar to the approach described by Bostock (1999), yet differs with respect to how the differential (or local) R/T matrix coefficients are evaluated. The approach of Bostock (1999) evaluates the differential R/T matrix coefficients via finite material property perturbations within a homogeneous reference medium. Here we describe and apply the approach of Thomson (1996a,b), where the differential R/T matrix coefficients are evaluated via products of the spatially localized eigenvector matrices of displacement and stress, and their derivatives with respect to depth.

Development of the R/T coefficients for continuously–variable media begins with equation 3.15 for a finite layer from z_1 to z_2. Differentiating with respect to z_2 we have

$$\frac{\partial}{\partial z_2}\left[\mathbf{N}(z_2)\begin{pmatrix}\mathbf{R}_U & \mathbf{T}_D\\ \mathbf{I} & 0\end{pmatrix}\right] = \frac{\partial}{\partial z_2}\left[\mathbf{P}(z_2,z_1)\mathbf{N}(z_1)\begin{pmatrix}0 & \mathbf{I}\\ \mathbf{T}_U & \mathbf{R}_D\end{pmatrix}\right] . \tag{3.26}$$

Noting that $\mathbf{N}(z_1)$ is independent of z_2, utilizing the equation of motion $d\mathbf{P}/dz = \mathrm{i}\omega\mathbf{A}\mathbf{P}$ and given the following initial values as $z_2 \to z_1$

$$\mathbf{P}(z_2,z_1), \mathbf{T}_U, \mathbf{T}_D \to \mathbf{I} \quad \text{and} \quad \mathbf{R}_U, \mathbf{R}_D \to \mathbf{0} , \tag{3.27}$$

equation 3.26 can be written

$$\begin{pmatrix}\partial_z\mathbf{t}_D & \partial_z\mathbf{r}_U\\ -\partial_z\mathbf{r}_D & -\partial_z\mathbf{t}_U\end{pmatrix} = \mathrm{i}\omega\mathbf{q} - \mathbf{N}^{-1}\partial_z\mathbf{N} . \tag{3.28}$$

The quantities $\mathbf{r}_{D,U}$ and $\mathbf{t}_{D,U}$ represent the local vertical derivatives of the 'thin' layer R/T coefficients. In effect, equation 3.28 is an expression for the local vertical derivatives of the global R/T coefficients. The quantities $\mathbf{q}$ and $\mathbf{N}^{-1}$ are known but an expression for $\partial_z\mathbf{N}$ is still needed. Two options are available to evaluate $\partial_z\mathbf{N}$: seek an analytic expression or approximate the expression numerically.

3.2.1 Analytic form

An analytic expression can be found by first taking the following derivative (equation 6.2 in Appendix A) with respect to z

$$\partial_z(\mathbf{A}\mathbf{N}) = \partial_z(\mathbf{N}\mathbf{q}) \tag{3.29}$$

yielding

$$\mathbf{q}\mathbf{B} - \mathbf{B}\mathbf{q} = \partial_z\mathbf{q} - \mathbf{N}^{-1}\partial_z\mathbf{A}\mathbf{N}, \tag{3.30}$$

where

$$\mathbf{B} = \mathbf{N}^{-1}\partial_z\mathbf{N} . \tag{3.31}$$

Equation 3.31 is referred to as the coupling matrix (Chapman, 2004). Expression 3.30 has the useful property in that the diagonal components are zero when $\mathbf{N}$ is normalized to the vertical energy flux. This can be seen by taking the derivative of equation 6.12 with respect to z,

$$\begin{aligned}\partial_z(\mathbf{N}^T\mathbf{J}\mathbf{N}) &= \partial_z(\mathbf{N}^T)\mathbf{J}\mathbf{N} + \mathbf{N}^T\mathbf{J}(\partial_z\mathbf{N})\\ &= (\partial_z\mathbf{N}^T)(\mathbf{N}^{-1})^T + \mathbf{N}^{-1}\partial_z\mathbf{N}\\ &= (\mathbf{N}^{-1}\partial_z\mathbf{N})^T + \mathbf{N}^{-1}\partial_z\mathbf{N}\\ &= \mathbf{B}^T + \mathbf{B} = \mathbf{0} .\end{aligned} \tag{3.32}$$

The result of which indicates that $\mathbf{B}$ is antisymmetric and thus the diagonal elements of $\mathbf{N}^{-1}\partial_z\mathbf{N}$ must be zero. That being the case, only the off–diagonal components need be determined and can be found from equation 3.30 as follows,

$$B_{ij} = \begin{cases} 0 & i = j\\ \frac{(\partial_z\mathbf{q} - \mathbf{N}^{-1}\partial_z\mathbf{A}\mathbf{N})_{ij}}{(q_i - q_j)} & i \neq j \end{cases} , \tag{3.33}$$

where $\partial_z\mathbf{A}$ and $\partial_z\mathbf{q}$ have yet to be evaluated.

The derivative of the system matrix $\mathbf{A}$ with respect to z is

$$\partial_z\mathbf{A} = \partial_z\begin{pmatrix}\mathbf{T}^T & \mathbf{C}_{33}^{-1}\\ \mathbf{S} & \mathbf{T}\end{pmatrix} \tag{3.34}$$

and can be expressed in terms of its partitions. The derivative $\partial_z\mathbf{C}_{33}^{-1}$ is found by making use of the relation $\mathbf{C}_{33}\mathbf{C}_{33}^{-1} = \mathbf{I}$ such that

$$\partial_z(\mathbf{C}_{33}\mathbf{C}_{33}^{-1}) = (\partial_z\mathbf{C}_{33})\mathbf{C}_{33}^{-1} + \mathbf{C}_{33}(\partial_z\mathbf{C}_{33}^{-1}) = \mathbf{0} \tag{3.35}$$

which yields

$$\partial_z\mathbf{C}_{33}^{-1} = -\mathbf{C}_{33}^{-1}(\partial_z\mathbf{C}_{33})\mathbf{C}_{33}^{-1}. \tag{3.36}$$

The remaining partition derivatives (after some simplification) are

$$\partial_z\mathbf{T} = \partial_z(-p_\gamma\mathbf{C}_{\gamma 3}\mathbf{C}_{33}^{-1}) \tag{3.37}$$

$$= -p_\gamma\left[(\partial_z\mathbf{C}_{\gamma 3})\mathbf{C}_{33}^{-1} - \mathbf{C}_{\gamma 3}\mathbf{C}_{33}^{-1}(\partial_z\mathbf{C}_{33})\mathbf{C}_{33}^{-1}\right]$$

$$\partial_z\mathbf{T}^T = (\partial_z\mathbf{T})^T \tag{3.38}$$

$$\begin{aligned}\partial_z\mathbf{S} &= \partial_z\left[\rho\mathbf{I} - p_\gamma p_\alpha\left(\mathbf{C}_{\alpha\gamma} - \mathbf{C}_{\alpha 3}\mathbf{C}_{33}^{-1}\mathbf{C}_{3\gamma}\right)\right]\\ &= \partial_z\rho\mathbf{I} - p_\gamma p_\alpha\left[(\partial_z\mathbf{C}_{\alpha\gamma}) - \right.\\ &\quad (\partial_z\mathbf{C}_{\alpha 3})\mathbf{C}_{33}^{-1}\mathbf{C}_{3\gamma} - \mathbf{C}_{\alpha 3}\mathbf{C}_{33}^{-1}(\partial_z\mathbf{C}_{33})\mathbf{C}_{33}^{-1}\mathbf{C}_{3\gamma}\\ &\quad \left. - \mathbf{C}_{\alpha 3}\mathbf{C}_{33}^{-1}(\partial_z\mathbf{C}_{3\gamma})\right] .\end{aligned} \tag{3.39}$$

There are several approaches which may be used to evaluate the derivative of the eigenvalue matrix $\mathbf{q}$ with respect to z. One approach would be to differentiate the solution to the eigenvalue problem

$$\partial_z\left[\det|\mathbf{A} - \mathbf{q}\mathbf{I}|\right] = 0 , \tag{3.40}$$

since $\partial_z\mathbf{A}$ is already known. Unfortunately this would be rather tedious since it requires evaluating the derivative of the cofactor matrices (Červený, 2001; Chapman, 2004). For 1–D media the lateral slownesses (p_α) remain constant with position $\mathbf{x}$. At any point $\mathbf{x}$ the corresponding vertical slownesses $\pm p_z$ for each wavetype are evaluated from the lateral

slownesses (p_α) and elastic matrix. Thus for all six possible waves the ray equations (Červený, 2001) can be used to evaluate $\partial_z \mathbf{q}$ from

$$\frac{\partial p_z}{\partial z} = -\left(\frac{\partial p_z}{\partial \tau} / \frac{\partial z}{\partial \tau}\right) \ , \tag{3.41}$$

where $\partial p_z/\partial\tau$ and $\partial_z/\partial\tau$ are evaluated using the ray equations.

It is now possible to solve the coupling matrix $\mathbf{B}$ using relation (3.33) which is clearly only valid if $q_i \neq q_j$. It is obvious that B_{ij} is singular along the diagonal, where $q_i = q_j$ and the denominator is zero. Since the coupling matrix describes how rapidly the eigenvector of the i*th* wave is changing with respect to that of the j*th* wave, the diagonal elements are not significant and can be set to zero.

Coupling occurs at interfaces and in regions of gradients, and is strongest within gradients when the wave slownesses are approximately equal. For anisotropic media, singularities will exist when the slowness sheets touch and special consideration must be taken (e.g., see Crampin & Yedlin, 1981; Shearer & Chapman, 1989; Angus et al., 2004, for intersection, kiss and conical point singularities). For the 1–D laterally isotropic case we can make use of the fact that the S_H–wave is invariant and so derivatives of both the displacement and stress eigenvector are zero. In other words, there is no coupling between the S_H–wave and the P– and S_V–waves in isotropic media. This implies that two eigenvectors (columns) associated with the S_H–waves be zero and, by making use of symmetry properties, determines the coupling matrix.

3.2.2 Numerical approximation

Evaluation of the analytic expression can be problematic when the model consists of a transition from isotropy to anisotropy, where the denominator in equation 3.33 becomes numerically singular as the medium approaches isotropy. An alternative to the analytic expression is to evaluate the derivative numerically using a first–order accurate finite–difference stencil, e.g.,

$$\partial_z \mathbf{N} \approx \frac{N_{z_i^+} - N_{z_i^-}}{\Delta z} + O\left(\Delta z\right) \ . \tag{3.42}$$

This approach is robust in terms of transitions between isotropy and anisotropy and is sufficiently accurate when Δz is not too large. However, implementation of this approach can be tricky when using the Runge–Kutta numerical approach, where variable step size is implemented (see next section for discussion of the Runge–Kutta method).

3.2.3 The Ricatti equations

Using either the analytic form (3.31) or numerical approximation (3.42) of $\partial_z \mathbf{N}$, the derivatives of equation 3.28 yield the approximate local vertical–gradient R/T coefficients for a thin layer to first–order with respect to thickness. These derivatives may be used with the addition rules 3.22–3.25 to obtain the global vertical–gradient R/T coefficients for a continuously–varying medium

$$\begin{aligned} d\mathbf{T}_U &= d\mathbf{t}_u \mathbf{T}_U + \mathbf{R}_D d\mathbf{r}_U \mathbf{T}_U \\ d\mathbf{T}_D &= \mathbf{T}_D d\mathbf{t}_D + \mathbf{T}_D d\mathbf{r}_U \mathbf{R}_D \\ d\mathbf{R}_U &= \mathbf{T}_D d\mathbf{r}_U \mathbf{T}_U \\ d\mathbf{R}_D &= d\mathbf{r}_D + d\mathbf{t}_U \mathbf{R}_D + \mathbf{R}_D d\mathbf{t}_D + \mathbf{R}_D d\mathbf{r}_U \mathbf{R}_D \end{aligned} \tag{3.43}$$

(Thomson, 1996b). These are the Ricatti equations and are a set of non–linear first–order ordinary differential equations (similar forms have been presented by Ursin, 1983; Tromp & Snieder, 1989; Bostock, 1999).

4 NUMERICAL IMPLEMENTATION

The numerical solution of the first–order non–linear Ricatti equations (3.43) can be solved by a variety of ordinary–differential equation solvers. Problems involving ordinary differential equations, such as the Ricatti equations, can be reduced to the study of a set of first–order differential equations of the form

$$\mathbf{y}' = \frac{d\mathbf{y}}{dz} = \mathbf{f}(z, \mathbf{y}) \tag{4.1}$$

with initial condition

$$\mathbf{y}(z_0) = \mathbf{\Gamma} \ . \tag{4.2}$$

The problem is then reduced to the study of a set of N coupled first–order differential equations. For the particular case of the Ricatti equations 3.43, the problem is reduced to a set of four coupled first–order equations of the form

$$\begin{aligned} \frac{d\mathbf{y}_1}{dz} &= \mathbf{a}_1(z)\mathbf{y}_1 + \mathbf{y}_4\mathbf{a}_3(z)\mathbf{y}_1 \\ \frac{d\mathbf{y}_2}{dz} &= \mathbf{y}_2\mathbf{a}_2(z) + \mathbf{y}_2\mathbf{a}_3(z)\mathbf{y}_4 \\ \frac{d\mathbf{y}_3}{dz} &= \mathbf{y}_2\mathbf{a}_3(z)\mathbf{y}_1 \\ \frac{d\mathbf{y}_4}{dz} &= \mathbf{a}_4(z) + \mathbf{a}_1(z)\mathbf{y}_4 + \mathbf{y}_4\mathbf{a}_2(z) + \mathbf{y}_4\mathbf{a}_3(z)\mathbf{y}_4 \end{aligned} \tag{4.3}$$

where

$$(\mathbf{y}_1, \mathbf{y}_2, \mathbf{y}_3, \mathbf{y}_4) = (\mathbf{T}_U, \mathbf{T}_D, \mathbf{R}_U, \mathbf{R}_D) \tag{4.4}$$

and

$$(\mathbf{a}_1, \mathbf{a}_2, \mathbf{a}_3, \mathbf{a}_4) = (d\mathbf{T}_U, d\mathbf{T}_D, d\mathbf{R}_U, d\mathbf{R}_D) \ . \tag{4.5}$$

Given the initial conditions

$$\mathbf{y}_1(z_o) = \mathbf{y}_2(z_o) = \mathbf{I} \qquad \text{and} \qquad \mathbf{y}_3(z_o) = \mathbf{y}_4(z_o) = \mathbf{0} \tag{4.6}$$

equations 4.3 can be solved numerically.

There are a variety of numerical approaches based on Euler's method to solve this system of first–order ordinary differential. In all approaches, the ordinary differential equation y' over an interval $z \in [a, b]$ is replaced by an algebraic equation of the form

$$\sum_{j=0}^{k} \alpha_j y_{n+j} = h\phi_f\left(y_{n+k}, y_{n+k-1}, \ldots, y_n, z_n; h\right) \tag{4.7}$$

at discrete points z_n defined by $z_n = a + nh$, where $n = 0, 1, 2, \ldots, N = (b-a)/h$ and the step length h may or may not vary (Lambert, 1991). The parameter ϕ_f is dependent on y_{n+k}, y_{n+k-1}, $\ldots$, y_n, $z_n$through the derivative function $f(z, y)$. The major branching point of these numerical methods is whether or not the one–step format is maintained. Linear multistep methods achieve higher accuracy by increasing the number of steps but retaining linearity in

terms of the y_{n+j} and $f_{n+j}, j = 0, 1, \ldots, k$ parameters. Bostock (1999) uses the Adams–Moulton implicit predictor–corrector multistep method to solve the Ricatti equations. In the formulation of Bostock (1999) the material properties are found through model perturbations and not though any direct explicit relationship to the independent variable z. Since the matrix coefficients are evaluated in a process independent of depth, the choice of the implicit predictor–corrector method is suitable. Furthermore, the predictor–corrector method has been observed to be relatively efficient for complicated functional forms of equations 3.43 (Bostock, personal communication, 1999).

In this paper, the formulation of the differential R/T matrix coefficients involves the products of depth localized eigenvector matrices and their derivatives. Since the derivation of the differential R/T matrix coefficients are explicitly related to the independent variable z, an ideal approach would involve implementation of a variable step length. Although predictor–corrector methods do allow for variable step length, they tend to be difficult to implement and less efficient than Runge–Kutta (RK) methods. RK methods retain the one–step format, but achieve higher order accuracy by sacrificing the linearity with respect to y_{n+j} and f_{n+j}. Although there is no difficulty in varying step length, error estimation can be more complicated to evaluate compared to linear multistep methods. However, for the derivation of the R/T coefficients in this paper, the RK method is more suitable since it can efficiently drive the step length and hence the depth at which the coefficients and their derivatives are evaluated. Changing step length can be easily accommodated since the dependent variables are explicitly described in terms of depth. This can be particularly important in regions with sharp gradients. [Other approaches that allow variable step size, such as the Bulirsch–Stoer algorithm (Press et al., 2007), may also be appropriate.] The specific RK method used in this study is Verner's eight–stage formula pair of order 5 and 6 (Verner, 1990, 1991). This method is a modification of Fehlberg's eight–stage formula pairs of order 5 and 6. The design has been modified such that the sixth–order approximation can be propagated using only eight function evaluations in each successful step (sometimes referred to as local extrapolation). Verner's 5–6 pair is found to be a suitable and convenient choice of RK method for solving the non–linear Ricatti equations.

5 RESULTS

We examine three 1–D Earth models based on the integral error function

$$erf(\eta) = \frac{2}{\pi} \int_0^{\eta} \exp\left[-(\eta')^2\right] d\eta' \tag{5.1}$$

(e.g., see equation 4–111, Turcotte & Schubert, 1982) commonly used as a solution in numerous physical problems. These models represent simple conceptual models of the asthenosphere–lithosphere transition (see Figure 3). The depth extent of the entire model as well as the thickness of the lithosphere are kept constant at 200 km and 50 km, respectively, and only the transition thickness below the lithosphere is varied. Model 1 is an isotropic transition consisting of a velocity increase between the asthenosphere and

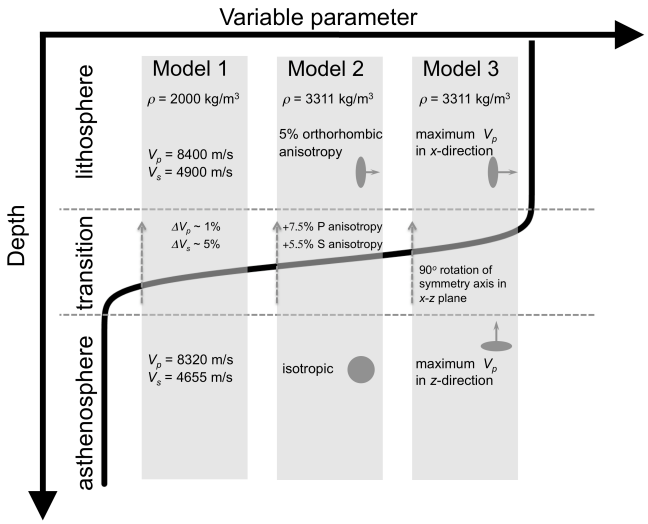

Figure 3. Sketch of the three simple 1–D models of an asthenosphere–lithosphere transition. The models are described from the bottom up to be consistent with the direction of propagation of the incident and converted waves. The variable parameter in model 1 is the isotropic velocity, in model 2 is the strength of anisotropy, and in model 3 is the orientation of the anisotropic symmetry axis. For simplicity, we consider constant density throughout the asthenosphere and lithosphere.

lithosphere, where the P–wave and S–wave velocities increase by 1% and 5%, respectively (based on Table 2 in Artemieva, 2009). Model 2 is a transition from isotropy to anisotropy, with isotropy in the asthenosphere developing into anisotropic olivine in the lithosphere. The olivine is scaled to a maximum P– and S–wave anisotropy of approximately 7.5% and 5.5%, respectively, and the isotropic elastic tensor is obtained using a Voigt–Reuss–Hill average (the orthorhombic olivine elasticity tensor is taken from Babuska & Cara, 1991, page 49). The transition from isotropy to anisotropy is accomplished by using the error function to define the anisotropic scaling. For this transition, the change in vertical P–wave velocity is minimal ($\Delta V_P \leq 0.2\%$), whereas the S–wave velocity for vertical propagation and horizontal polarization increases by up to 3%. Model 3 is entirely anisotropic (7.5% and 5.5% P– and S–wave anisotropy) in both the asthenosphere and lithosphere and is loosely based on the studies of Ben Ismaïl & Mainprice (1998) and Blackman & Kendall (2002). The gradient is defined by a smooth rotation of the olivine elastic tensor. In the lithosphere, the fast P–wave velocity is aligned along the x–axis, the slow P–wave velocity along the y–axis and the moderate P–wave velocity along the z–axis. In the asthenosphere, the fast and moderate P–wave velocities are rotated (i.e., fast P–wave along the z–axis and the moderate P–wave along the x–axis). See Table 2 for elastic tensor coefficients for models 2 and 3.

In model 1, the analytic form of the coupling matrix (3.31) is used since there is no transition between isotropy and anisotropy. However, for the anisotropic transitions, the numerical approximation of the coupling matrix (3.42) is used. This is because model 2 consists of a transition from isotropy to anisotropy and, in model 3, we may expect re-

Model		C_{11}	C_{22}	C_{33}	C_{12}	C_{13}	C_{23}	C_{44}	C_{55}	C_{66}
2	Litho	77.616	77.616	70.560	24.314	25.944	25.944	24.010	24.010	26.651
	Asthe	70.560	70.560	70.560	22.540	22.540	22.540	24.010	24.010	24.010
3	Litho	77.616	77.616	70.560	24.314	25.944	25.944	24.010	24.010	26.651
	Asthe	70.560	77.616	77.616	25.944	25.944	24.3140	26.651	24.010	24.010

Figure 2. Elastic tensor components (in GPa) for the anisotropic models 2 and 3. The elastic tensors are density normalized, where density $\rho = 3311$ kg/m^3.

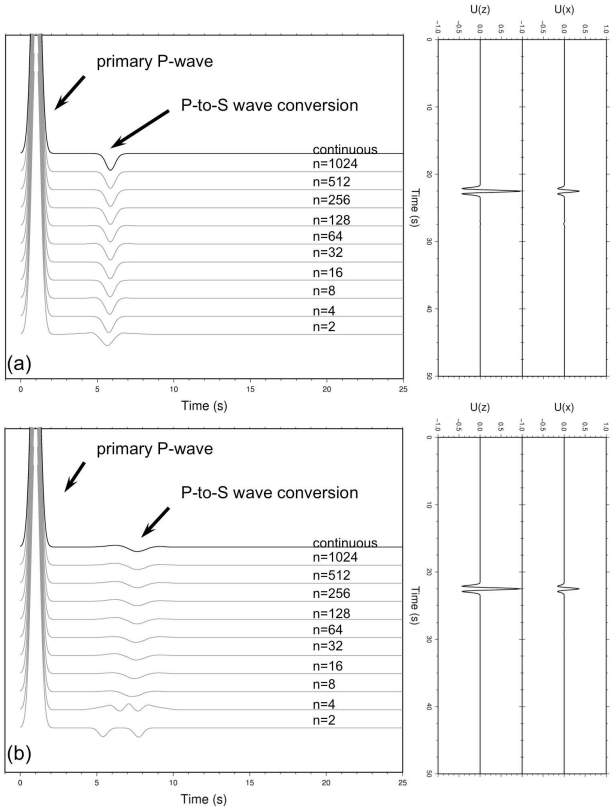

Figure 4. Results for model 1 (isotropic transition) for incident P–wave: (a) 10 km transition and (b) 50 km transition. For this and remaining figures, the left column displays the receiver function signals and the right column displays the vertical ($U(Z)$) and horizontal ($U(X)$) displacement waveforms. The grey waveforms are from the discontinuous models, where n refers to the number of discrete layers, and the waveforms in black are from the continuous model (or Ricatti solution). Note that the primary waveforms are clipped to enhance the converted phase waveforms. As well, the amplitude of the receiver functions in Figures 3, 4 and 5 have been scaled by a factor of 2 to improve visualization of the converted waveforms.

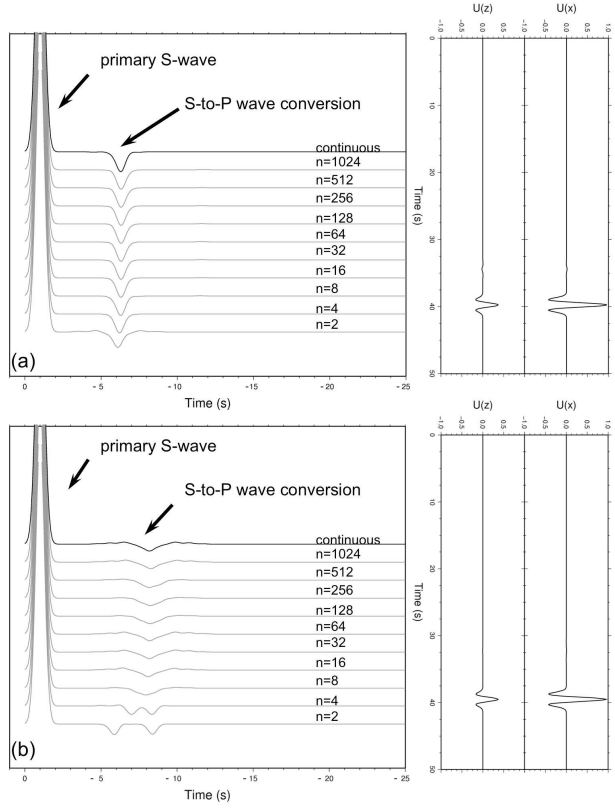

Figure 5. Results for model 1 (isotropic transition) for incident S–wave: (a) 10 km transition and (b) 50 km transition.

gions containing S–wave slowness surface singularities to exist.

Typical epicentral distances used in receiver function analysis range between 35° and 95° for P receiver functions (e.g., Wilson et al., 2005) and between 60° and 75° for S receiver functions (e.g., Wilson et al., 2006; Angus et al., 2006). Based on these epicentral distances, we use an incidence angle of 20° from vertical as representative of vertical incidence for both teleseismic P– and S–waves. We model the seismic source as a plane–wave with a Ricker wavelet having dominant (or peak) frequency of 1 Hz and 0.5 Hz for incident P– and S–waves, respectively. Based on the velocities used in the models (8.4 km/s for P-wave and 4.9 km/s for S-wave), the wavelengths of the P– and S–waves are approximately 8.4 km and 9.8 km, respectively. For dominant wavelengths on the order of 10 km for both wave types, two transition thicknesses are considered; a 50 km transition (e.g., representative of a diffuse thermal anomaly) and a 10 km transition (e.g., representative of a zone of partial melt or hydration). For all models, we present the deconvolved converted waveforms using the iterative time–domain technique of Ligorria & Ammon (1999) [for P–to–S conversion, we deconvolve the z–component (vertical) from the x–component, and for S–to–P conversion, we deconvolve the x–component from the z–component and reverse the time axis such that the converted P–wave trails the incident S–wave].

The transmission results for model 1 (isotropic LAB) are shown in Figures 4 and 5. For the 10 km transition, the

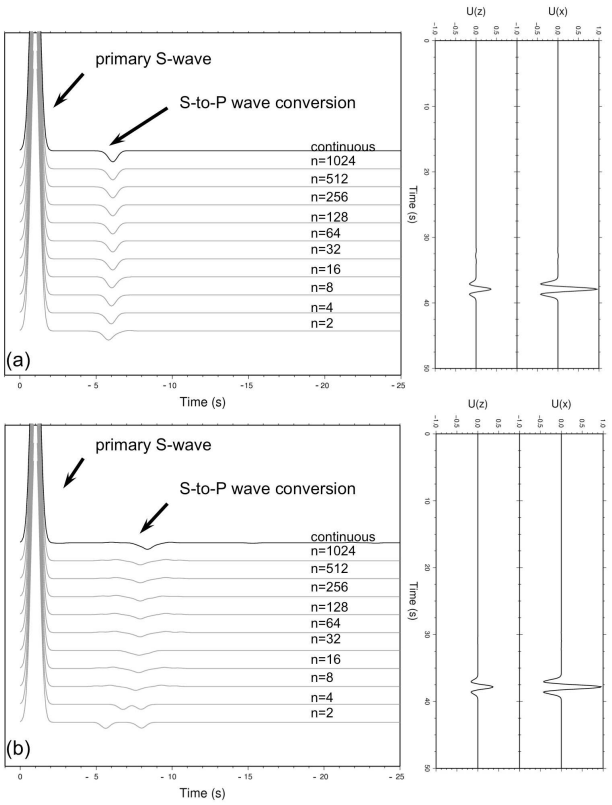

Figure 6. Results for model 2 (isotropic to anisotropic) transition for incident S–wave: (a) 10 km transition and (b) 50 km transition.

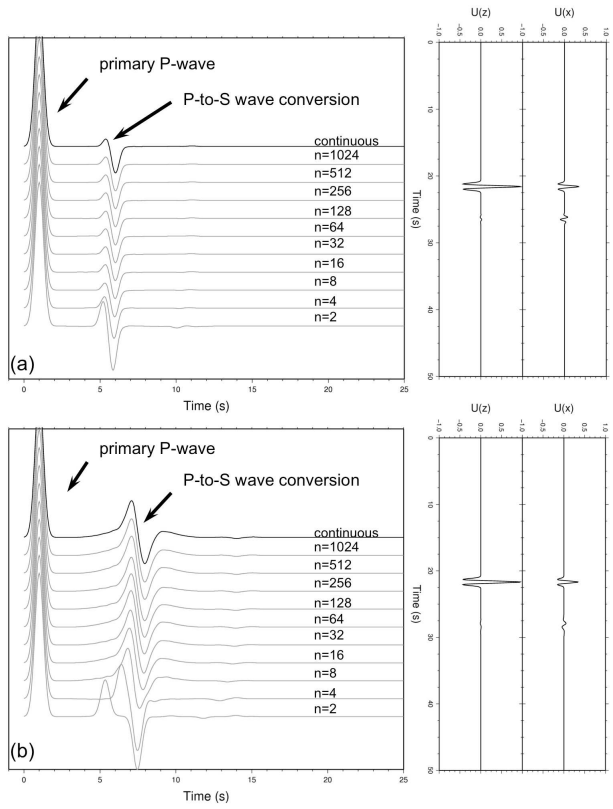

Figure 7. Results for model 3 (rotation of anisotropic symmetry) for incident P–wave: (a) 10 km transition and (b) 50 km transition.

discontinuous transitions (n=2 to n=1024) are in general agreement with the continuous transition model. However, there is a slight phase discrepancy for models n=2 and n=4, and the converted signal for discontinuous model n=2 shows a broader pulse. For this weak velocity transition, the results are in agreement with previous studies that suggest a transition layer thickness on the order of 1/8 the seismic wavelength is sufficiently accurate. For typical signal–to–noise ratios in real teleseismic receiver functions and considering that receiver functions are often stacked, modelling a 10 km transition using a discrete jump in material properties may be adequate (i.e., n=2) [often this is the case for most receiver function modelling]. For the 50 km transition, accurate modelling of mode conversion requires at least 8 discrete layers and this suggests a minimum discontinuous transition thickness of approximately 1/2 the dominant wavelength.

The transmission results for model 2 (isotropic to anisotropic transition) are shown in Figure 6. Since the change in vertical P–wave velocity for this model is very small ($\approx 0.2\%$), we only show the results for an incident S–wave (i.e., P–to–S mode conversion is negligible). The simulations for this model are almost identical to those of model 1 (see Figure 5), with the exception of smaller converted wave amplitudes due to the smaller velocity gradient.

The transmission results for model 3 (rotation of anisotropy) are shown in Figures 7 and 8. For the 10 km transition for both P and S incident waves, the discontinuous transitions for n=16 to n=1024 are consistent with the continuous transition receiver functions. For transition models n=4 to n=8 there are some slight differences in the waveform shape and for n=2 the discontinuous transition yields a noticeable difference in amplitude and pulse. For the 50 km transition, the P–to–S and S–to–P mode conversions are best modelled with at least n=16 discrete layers. However, only at n=128 do the waveforms of the discontinuous model match the continuous transition results in Figure 8(b).

Thus a conservative criterion would be discrete transition layer thicknesses on the order of 1/20 the dominant seismic wavelength. However, again considering noise considerations and stacking procedures, it is fair to say that discrete transition layer thicknesses on the order of 1/3– to 1/8 the dominant seismic wavelength are sufficient for receiver function studies.

6 CONCLUSIONS

We have presented a derivation of the R/T response for 1–D, continuously–varying, generally anisotropic elastic media in the form of the Ricatti equations and have discussed the numerical implementation of these Ricatti equations to obtain plane–wave R/T synthetics for continuous elastic gradients. We have compared numerical results for three 1–D discontinuous and continuous transitions for both isotropic and anisotropic media. The results suggest that discontinuous representations with layer thicknesses on the order of 1/3 to 1/8 the dominant seismic wavelength can be used to accu-

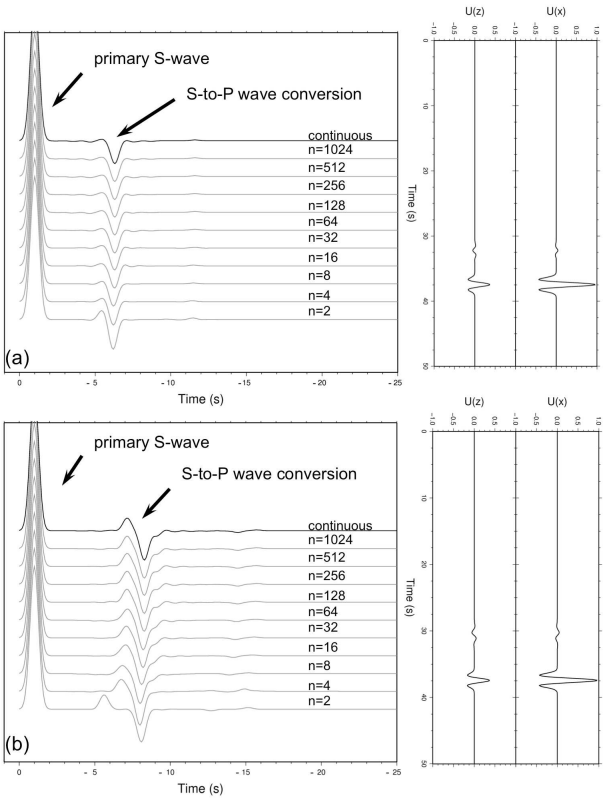

Figure 8. Results for model 3 (rotation of anisotropic symmetry) for incident S–wave: (a) 10 km transition and (b) 50 km transition.

rately model mode conversions from continuous transitions in isotropic and anisotropic elastic properties. In terms of application to receiver function studies of the lithosphere–asthenosphere boundary, the results indicate that accurate mode converted synthetics due to continuous elastic gradients can be modelled with discontinuous gradient representations with layer thicknesses of up to 1/3 to 1/2 the dominant seismic wavelength (when considering the influence of signal noise and the impact of stacking procedures on composite receiver functions).

It should be noted that the models considered in this study are simple representations of the LAB and so it remains to be considered what influence slowness surface singularities might have with respect to the genesis and behaviour of converted waves. However, the results indicate that discontinuous representations of continuous transitions via a reasonable number of discrete layers can be used to generate relatively accurate synthetics. This has important implications in terms of the computational efficiency of reflectivity modelling algorithms not only for plane–wave synthetics but, more importantly, for solutions consisting of a spectrum of slownesses.

ACKNOWLEDGMENTS

Both DAA and CJT would like to thank Professor Vlastislav Červený for his lifelong dedication to seismic ray theory and sharing his knowledge in a clear and concise manner. The development and implementation of the R/T coefficients in this study originated from DAA's PhD degree course work in 1999 while at Queen's University, Kingston, Canada. Therefore DAA would like to thank Professor Jim Verner for offering, for one last time, his course on Numerical Treatment of Initial Value Problems in Ordinary Differential Equations as well as his guidance with the Runge–Kutta method. DAA would also like to thank Professor Michael Bostock for discussion on the numerical implementation of the Ricatti equations.

References

Angus, D.A. (2004) *Development and application of one-way elastic wave propagators in generally anisotropic, heterogeneous, 3D media*, Ph.D. thesis, Queen's University, Canada.

Angus, D.A., C.J. Thomson and R.G. Pratt (2004) A one-way wave equation for modelling seismic waveform variations due to elastic anisotropy, *Geophysical Journal International*, **156**(3), 595–614.

Angus, D.A. (2005) A one–way wave equation for modelling seismic waveform variations due to elastic heterogeneity, *Geophys. J. Int.*, **162**, 882–898.

Angus, D.A. (2007) True amplitude corrections for a narrow–angle one–way elastic wave equation, *Geophysics*, **72** (2), T19–T26.

Angus, D.A., D.C. Wilson, E. Sandvol and J.F. Ni (2006) Lithospheric structure of the Arabian and Eurasian collision zone in eastern Turkey from S-wave receiver functions, *Geophys. J. Int.*, **166**, 1335–1346.

Angus, D.A., J–M. Kendall, D.C. Wilson, D.J. White, S. Sol and C.J. Thomson (2009) Stratigraphy of the Archean western Superior Province from P- and S-wave receiver functions: Further evidence for tectonic accretion?, *Phys. Earth Planet. In.*, **177**, 206–216.

Artemieva, I.M. (2009) The continental lithosphere: reconciling thermal, seismic, and petrologic data, *Lithos*, **109**, 23–46.

Audet, P., M.B. Bostock and J–P. Mercier (2007) Teleseismic waveform modelling with a one-way wave equation, *Geophys. J. Int.*, **171**, 1212–1225.

Babuska, V. and M. Cara (1991) *Seismic anisotropy in the Earth*, Kluwer Academic Publishers, London.

Ben Ismaïl, W. and Mainprice, D. (1998) An olivine fabric database: an overview of upper mantle fabrics and seismic anisotropy, *Tectonophysics*, **296**, 145–157.

Blackman, D.K. and J–M. Kendall (2002) Seismic anisotropy in the upper mantle 2. Predictions for current plate boundary flow models, *Geochem. Geophys. Geosyst.*, **3**(9), 1–26.

Bostock, M.G. (1999) Seismic waves converted from velocity gradient anomalies in the Earth's upper mantle, *Geophys. J. Int.*, **138**, 747–756.

Brenders, A.J. and R.G. Pratt (2007) Full waveform tomography for lithospheric imaging: results from a blind test in a realistic crustal model, *Geophys. J. Int.*, **168**, 133–151.

Červený, V. (2001) *Seismic ray theory*, Cambridge University Press.

Chapman, C.H. (2004) *Fundamentals of seismic wave propagation*, Cambridge University Press.

Chapman, C.H. and P.M. Shearer (1989) Ray tracing in azimuthally anisotropic media–II. Quasi–shear wave coupling, *Geophysical Journal International*, **96**, 65–83.

Coates, R.T. and C.H. Chapman (1990) Quasi–shear wave coupling in weakly anisotropic 3–D media, *Geophysical Journal International*, **103**, 301–320.

Crampin, S. and M. Yedlin (1981) Shear–wave singularities of wave propagation in anisotropic media, *Journal of Geophysics*, **49**, 43–46.

Farra, V. and L. Vinnik (2000) Upper mantle stratification by P and S receiver functions, *Geophys. J. Int.*, **141**, 699-712.

Fischer, K.M., H.A. Ford, D.L. Abt and C.A. Rychert (2010) The lithosphere–asthenosphere boundary, *Annu. Rev. Earth Planet Sci.*, **38**, 551–575.

Frederiksen, A.W. and M.G. Bostock (2000) Modelling teleseismic waves in dipping anisotropic structures, *Geophys. J. Int.*, **141**, 401–412.

Fryer, G.J. and L.N. Frazer (1984) Seismic waves in stratified anisotropic media, *Geophys. J. R. astr. Soc.*, **78**, 691–710.

Fuchs, K. and G. Mueller (1971) Computation of synthetic seismograms with the reflectivity method and comparison with observations, *Geophys. J. R. astr. Soc.*, **23**, 417-433.

Garmany, J. (1983) Some properties of elastodynamic eigensolutions in stratified media, *Geophys. J. R. astr. Soc.*, **75**, 565–569.

Gilbert, F. and G.E. Backus (1966) Propagator matrices in elastic wave and vibration problems, *Geophysics*, **31**, 326–332.

Guest, W.S., C.J. Thomson and C.P. Spencer (1993) Anisotropic reflection and transmission calculations with application to a crustal seismic survey from the East Greenland Shelf, *J. Geophys. Res.*, **98**, 14161–14184.

Hammond, J.O.S., J-M. Kendall, D.A. Angus and J. Wookey (2010) Interpreting spatial variations in anisotropy: insights into the Main Ethiopian Rift from SKS waveform modelling, *Geophys. J. Int.*, **181**, 1701–1712.

Haskell, N.A. (1953) The dispersion of surface waves on multilayered media, *B.S.S.A.*, **43**, 17–34.

Helffrich, G., E. Asencio, J. Knapp and T. Owens (2003) Transition zone structure in a tectonically inactive area: 410 and 660 km discontinuity properties under the northern North Sea, *Geophys. J. Int.*, **155**, 193–199.

Helffrich, G., B. Faria, J. Fonseca, A. Lodge and S. Kaneshima (2008) Transition zone structure under a stationary hot spot: Cape Verde, *AGU Fall Meeting Abstracts*, DI52A–07.

Holtzman, B.K. and J–M. Kendall (2010) Organized melt, seismic anisotropy, and plate boundary lubrication, *Geochem. Geophys. Geosyst.*, **11**, 1–29.

Hudson, J.A. (1980) *The Excitation and Propagation of Elastic Waves*, Cambridge University Press.

Kennett, B.L.N. (1974) Reflections, rays and reverberations, *B.S.S.A.*, **64**, 685–696.

Kennett, B.L.N. (1983) *Seismic Wave Propagation in Stratified Media*, Cambridge University Press.

Kennett, B.L.N. (2001a) *The Seismic Wavefield, Volume 1: Introduction and Theoretical Development*, Cambridge University Press.

Kennett, B.L.N. (2001b) *The Seismic Wavefield, Volume 2: Interpretation of Seismograms on Regional and Global Scales*, Cambridge University Press.

Kuhn, M.J. (1988) Simulation of a velocity transition zone by a stack of thin homogeneous layers, *Geoexploration*, **25**, 1–11.

Kumar, P., X. Yuan, R. Kind and G. Kosarev (2005) The Lithosphere–asthenosphere boundary in the Tien Shan-Karakoram region from S receiver functions – Evidence of continental subduction, *Geophys. Res. Lett.*, **32**, L07305.

Lambert, J.D. (1991) *Numerical Methods for Ordinary Differential Systems*, John Wiley & Sons.

Langston, C.A. (1977) Corvallis, Oregon, crustal and upper mantle receiver structure from teleseismic P and S waves, *B.S.S.A.*, **67**, 713-724.

Li, X., R. Kind, X. Yuan, I. Wölbern and W. Hanka (2004) Rejuvenation of the lithosphere by the Hawaiian plume, *Nature*, **427**, 827-829.

Ligorria, J.P. and C.J. Ammon (1999), Iterative deconvolution and receiver–function estimation, *B.S.S.A.*, **89**, 1395-1400.

Molotkov, L.A., V. Červený, and O. Novotný (1976) Low–frequency and high–frequency expressions for the reflection and transmission coefficients of seismic waves for transition layers, *Stud. Geoph. et Geod.*, **20**, 219–235.

Novotný, O., V. Červený and L.A. Molotkov (1980) Numerical properties of low–frequency expansions for the reflection and transmission coefficients from transition layers, *Stud. Geoph. et Geod.*, **24**, 124–130.

Press, W.H., S.A. Teukolsky, W.T. Vetterling, and B.P. Flannery (2007) *Numerical Recipes: The Art of Scientific Computing*, 3rd edition. Cambridge University Press.

Rychert, C.A., K.M. Fischer and S. Rondenay (2005) A sharp lithosphere–asthenosphere boundary imaged beneath eastern North America, *Nature*, **436**, 542–545.

Saastamoinen, P. R. (1980) On propagators and scatterers in wave problems of layered, elastic media – a spectral approach, *B.S.S.A.*, **70**(4), 1125–1135.

Shearer, P.M. and C.H. Chapman (1988) Ray tracing in anisotropic media with a linear gradient, *Geophysical Journal*, **94**, 575–580.

Shearer, P.M. and C.H. Chapman (1989) Ray tracing in azimuthally anisotropic media–I. Results for models of aligned cracks in the upper crust, *Geophysical Journal*, **96**, 51–64.

Thompson, D.A., G. Helffrich, I.D. Bastow, J–M. Kendal, J. Wookey, D.W. Eaton and D.B. Snyder (2011) Implications of a simple mantle transition zone beneath cratonic North America, *E.P.S.L.*, **312**, 28–36.

Thomsen, L. (1986) Weak elastic anisotropy, *Geophysics*, **51**(1), 1954–1966.

Thomson, C.J. (1996a) *Notes on Rmatrix, a program to find the seismic plane–wave response of a stack of anisotropic layers*, Department of Geological Sciences, Queen's University, Canada.

Thomson, C.J. (1996b) *Notes on Waves in Layered Media to Accompany Program Rmatrix*, Department of Geological Sciences, Queen's University, Canada.

Tomlinson, J.P., P. Denton, P.K.H. Maguire and J.R. Evans (2003) UK crustal structure close to the Iapetus Suture: a receiver function perspective, *Geophys. J. Int.*, **154**, 659–

665.

Tromp, J. and R. Snieder (1989) The reflection and transmission of plane P- and S-waves by a continuously stratified band: a new approach using invariant imbedding, *Geophys. J.*, **96**, 447–456.

Turcotte, D.L. and G. Schubert (1982) *Geodynamics: Applications of Continuum Physics to Geological Problems*, John Wiley & Sons, New York.

Ursin, B. (1983) Review of elastic and electromagnetic wave propagation in horizontally layered media, *Geophysics*, **48**, 1063–1081.

Verner, J.H. (1990) A contrast of some Runge–Kutta formula pairs, *SIAM J. Num. Anal.*, **27**, 1332–1344.

Verner, J.H. (1991) Some Runge–Kutta formula pairs, *SIAM J. Num. Anal.*, **28**, 496–511.

Vinnik, L.P. (1977) Detection of waves converted from P to SV in the mantle, *Phys. Earth planet. Inter.*, **15**, 39–45.

Wilson, D., R. Aster, J. Ni, S. Grand, M. West, W. Gao, W.S. Baldridge and S. Semken (2005) Imaging the seismic structure of the crust and upper mantle beneath the Great Plains, Rio Grande Rift, and Colorado Plateau using receiver functions, *J. Geophys. Res.*, **110**, B05306.

Wilson, D.C., D.A. Angus, J.F. Ni and S.P. Grand (2006) Constraints on the interpretation of S-to-P receiver functions, *Geophys. J. Int.*, **165**, 969–980.

Woodhouse, J.H. (1973) Surface waves in a laterally varying layered structure, *Geophys. J. R. astr. Soc.*, **37**, 461–490.

Appendix A: Symmetry properties

The matrices $\mathbf{N}$ and $\mathbf{q}$ can be found using standard numerical techniques for eigenvector/eigenvalue solutions. It remains, however, to find the inverse of the eigenvector matrix $\mathbf{N}^{-1}$. Since $\mathbf{N}$ and $\mathbf{N}^{-1}$ are eigencolumn and eigenrow matrices, respectively, they must be related in a simple manner. If $\mathbf{a}_i$ is a column eigenvector (a column of $\mathbf{N}$) and $\mathbf{b}_i^T$ a row eigenvector (a row of $\mathbf{N}^{-1}$) then there exists a transformation $\mathbf{b}_i = \mathbf{J}\mathbf{a}_i$ such that $(\mathbf{N}^{-1}) = \mathbf{J}\mathbf{N}$. The transformation matrix

$$\mathbf{J}_1 = \begin{pmatrix} 0 & \mathbf{I} \\ \mathbf{I} & 0 \end{pmatrix} , \tag{6.1}$$

is important because it enables the determination of $\mathbf{N}^{-1}$ without having to resort to any numerical inversion scheme (Fryer & Frazer, 1984).

Further, the system matrix $\mathbf{A}$ contains a number of symmetries that can be utilized to reduce the amount of computation as well as to check results. These symmetries have been noted by Woodhouse (1974), Garmany (1983), and Fryer & Frazer (1984), to name a few. The eigenvector/eigenvalue problem,

$$\mathbf{A}\mathbf{N} = \mathbf{N}\mathbf{q} \tag{6.2}$$

has related equations

$$\mathbf{N}^T\mathbf{A}^T = \mathbf{q}\mathbf{N}^T \qquad \mathbf{N}^{-1}\mathbf{A} = \mathbf{q}\mathbf{N}^{-1} . \tag{6.3}$$

Since $\mathbf{A}$ has the following symmetry

$$(\mathbf{J}_1\mathbf{A}) - (\mathbf{J}_1\mathbf{A})^T = 0 \tag{6.4}$$

it is found that

$$\left(\mathbf{N}^T\mathbf{J}_1\right)\mathbf{A} = \mathbf{q}\left(\mathbf{N}^T\mathbf{J}_1\right) . \tag{6.5}$$

The inverse of $\mathbf{N}$ is thus

$$\mathbf{N}^{-1} = \mathbf{d}\mathbf{N}^T\mathbf{J}_1 , \tag{6.6}$$

where $\mathbf{d}$ is a diagonal matrix and its form depends on how $\mathbf{N}$ is normalized (if at all). It is possible to normalize so that $\mathbf{d}$ is the identity matrix, but more generally it may be found from the trivial diagonal inverse

$$\mathbf{d} = \left(\mathbf{N}^T\mathbf{J}_1\mathbf{N}\right)^{-1} . \tag{6.7}$$

One method of normalization, which is specifically utilized in this algorithm, makes use of the vertical energy flux (Červený, 2001). Each column $\mathbf{a}_i$ of $\mathbf{N}$ is an eigenvector of the form

$$\mathbf{a}_i = \mathbf{N}_i = \begin{pmatrix} \mathbf{u}_i \\ \mathbf{t}_i \end{pmatrix} \tag{6.8}$$

where, for each a_i,

$$\mathbf{u} = \begin{pmatrix} u_{x_1} \\ u_{x_2} \\ u_z \end{pmatrix} \quad \text{and} \quad \mathbf{t} = \frac{1}{i\omega}\begin{pmatrix} \sigma_{13} \\ \sigma_{23} \\ \sigma_{33} \end{pmatrix} . \tag{6.9}$$

The normalized form of $\mathbf{N}$ is written

$$\hat{\mathbf{N}}_i = \epsilon_i \begin{pmatrix} \mathbf{u}_i \\ \mathbf{t}_i \end{pmatrix} , \tag{6.10}$$

where

$$\epsilon_i = \left(\mathbf{t}_i^T\mathbf{u}_i + \mathbf{u}_i^T\mathbf{t}_i\right)^{-\frac{1}{2}} \tag{6.11}$$

is the vertical energy flux. This normalization is quite useful in that it results in the property

$$\mathbf{N}^T\mathbf{J}\mathbf{N} = \mathbf{I} . \tag{6.12}$$